Journal of Sensor Science and Technology
Vol. 34, No. 1 (2025) pp. 44-54
http://dx.doi.org/10.46670/JSST.2025.34.1.44
pISSN 1225-5475/eISSN 2093-7563

Structure of Photoacoustic Spectroscopy (PAS) Cells and Lock-in Amplifiers for PAS Gas Sensors: A Review-PART I

Seungoh Han[1] and SeungHwan Yi[2,+]

Abstract

In this study, photoacoustic spectroscopy (PAS) cells and lock-in amplifiers (LIAs) were surveyed to develop PAS gas sensors. PAS gas sensors are based on the physical principle of detection; therefore, the enhancement of their performance is affected by the related fundamental properties of target gas concentrations, absorption coefficients, cell setup constants, and power of the infrared light source. Among these, the optical path length, cell volume, and source power are the major factors that enhance the sensitivity of PAS gas sensors. In terms of LIAs, the vector analysis method is much simpler and more cost-effective than the phase-voltage conversion method. Furthermore, active analog–digital LIAs are promising circuitry for PAS gas sensors.

Keywords: Photoacoustic spectroscopy, PAS Cells, Gas sensors, Helmholtz resonator, White-cell, Lock-in amplifiers

1. INTRODUCTION

In 1880, Alexander Graham Bell discovered the phenomenon known as the photoacoustic effect. He found that when light was directed onto a rapidly moving disk with a slot and the light passing through the slot was focused onto a thin diaphragm, sound was produced [1]. The photoacoustic effect refers to the conversion of absorbed light energy into mechanical energy through an energy-transformation process in solids, liquids, and gases. However, owing to the lack of acoustic pressure sensors to measure the phenomena caused by light absorption and emission at the time, technological developments were limited. Furthermore, although Viegerov first applied the photoacoustic effect to gas analysis before the 1960s [2], the absence of an effective acoustic sensor hindered further progress. However, with the invention and application of technologies such as CO_2 and He-Ne lasers and the demonstration of trace gas measurements at parts per billion (ppb) concentrations [3,4], PAS gas sensors have gained renewed attention and have evolved to the present day.

Currently, gas sensors based on both chemical and physical methods are employed for the measurement of various trace gases. However, chemical gas sensors have several limitations. First, lack of selectivity, because the target gas undergoes combustion reactions simultaneously with various gases in the surrounding air at high temperatures. Consequently, the selective reactions and concentration analyses of specific gases are ongoing areas of research. Second, a recovery issue, as the surface that undergoes a chemical reaction has difficulty returning to its original state, and this process takes a significant amount of time. Third, stability and long-term reliability. Even if the sensor surface is periodically heated to oxidize the accumulated residues in the air, it is challenging to restore the surface to its initial state. This makes it difficult to overcome long-term reliability problems that require the periodic resetting of the initial state.

Physical methods, such as optical methods that utilize the gas absorption spectrum, can alleviate the issues associated with chemical methods. For example, nondispersive infrared gas sensors can be used to measure gases such as carbon dioxide, methane, respiratory alcohol levels, and transformer oil gas analysis [5-12]. However, they have the disadvantage of low resolution, tens of parts per million (ppm). In contrast, PAS gas sensors are more suitable for trace gas measurements (at concentrations below ppm) and have been widely used in various fields, including household electronics, gas monitoring, and transformer oil gas analysis, since the 2000s [13]. Additionally, optical gas sensors have been explored for the analysis of sub-

[1]Dep. of Intelligent Robotics, Hoseo University
20 hoseo-ro 79 Beongil, Baebang-eup, Asan-Si, Chungcheongnam-do, 31499, Republic of Korea
[2]Dep.of Mechanical Eng., College of Convergence Technology, Korea National University of Transportation
50, Daehakro, Chungjushi, Chungbuk, 27469, Republic of Korea
[+]Corresponding author: isaac_yi@ut.ac.kr
(Received: Dec. 23, 2024, Revised: Dec. 31, 2024, Accepted: Jan. 13, 2025)

ppm biomarkers (such as ethanol, methanol, acetone, and isopropyl alcohol) emitted from the human body [14].

This review explores the principles of PAS gas sensors, the characteristics that their key components must have, and methods for enhancing these characteristics, along with the types and features of lock-in amplifiers (LIAs), which are used as signal-processing circuits for the development of innovative PAS sensors.

2. PRINCIPLE AND STRUCTURES OF PAS GAS SENSORS

2.1 Principle and Categories of PAS Gas Sensors

Gas sensors are generally classified into physical and chemical types. Chemical gas sensors include semiconductors, contact combustion sensors, and electrolyte-based sensors. PAS gas sensors, a type of physical sensor, are further categorized into direct and indirect types [1,15]. The distinction between direct and indirect types is based on whether the generated signal (acoustic pressure) from the energy-conversion process in the optical path is measured. In the direct type, PAS sensors are divided into non-resonant [16] and resonant types [17-21]. Non-resonant PAS sensors simply include an optical waveguide and an acoustic pressure sensor, whereas resonant PAS sensors include components such as microphones, quartz resonators, or cantilever structures inside the PAS cell designed to resonate at specific frequencies. These sensor types are further categorized in terms of their structure and characteristics. The operating principle of the PAS gas sensor is as follows.

The gas detection principle of the PAS gas sensors follows the process shown in Fig. 1. When infrared light is emitted from a light source, the infrared radiation passes through an optical waveguide or resonator. Finally, the transmitted energy is measured using an optical detector to assess the degradation and transmitted energy of the light source. If a target gas is present in the optical path, it absorbs infrared light in a specific wavelength range based on its absorption coefficient (Table 1). The infrared light absorbed within a resonant optical waveguide is released as heat through a nonradiative relaxation process, which causes thermal vibrations in the surrounding gas molecules. This thermal energy results in changes in the acoustic pressure over time. Placing an acoustic sensor (e.g., microphone, cantilevers, or quartz tuning fork) in the area where thermal vibrations occur, the pressure change caused by the energy release process can be directly measured. This is referred to as a direct-type photoacoustic gas sensor, which typically has the structure shown in Fig. 2.

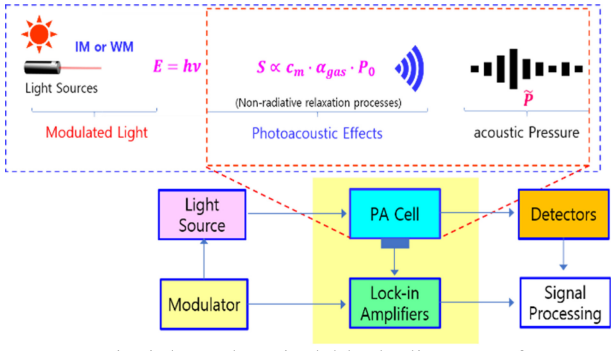

Fig. 1. Principle and typical block diagram of PAS gas sensor. Reprinted with permission from Ref. [16] Copyright (2022) Elsevier (IM: intensity modulation, WM: wavelength modulations).

Table 1. Absorption wavelength of target gases in the mid-infrared region adapted from [22] and additional data from [23].

Target gases	Absorption wavelength (μm)	
Butyrate	3.36/5.78/6.82 8.50/9.10/9.75	7.27/7.65/7.95
Acetone	5.80/7.30	
Propan-1-ol	3.36/3.40/3.47	9.45
Propan-2-ol	3.37/7.24/8.60	8.85/10.50
Toluene	3.29/6.65	
Ethylene Oxide	3.26	
Ethanol	3.35/3.45/9.38	
Methanol	3.36/9.45/9.85	
SO_2	7.35, 18.88	
CF_4	4.57/7.79	
CO_2	4.26/4.29	

In PAS gas sensor systems, the voltage generated by the acoustic pressure induced by light irradiation is given by Eq. (1) [24,2]:

$$S_p = C_{cell} M_s N_{tot} c_m \alpha_p P_0 = \frac{(\gamma - 1) LQ}{V_C \omega} M_S N_{tot} c_m \alpha_p P_0 \quad (1)$$

where C_{cell} is the constant defining the resonator's characteristics (Pa/m^{-1}W), γ is the adiabatic coefficient of the gas, L is the optical path length (m), Q is the quality factor, V_C is the volume of the PAS gas sensor cell (m^3), ω is the angular frequency (rad/s), M_S is the sensitivity of the acoustic sensor (mV/Pa), N_{tot} is the molecular density of the gas (molecules/m^3), c_m is the gas concentration (ppm), α_p is the spectral line intensity of the gas at the specific wavelength range (m/mol), and P_0 is the energy of the irradiated light (W).

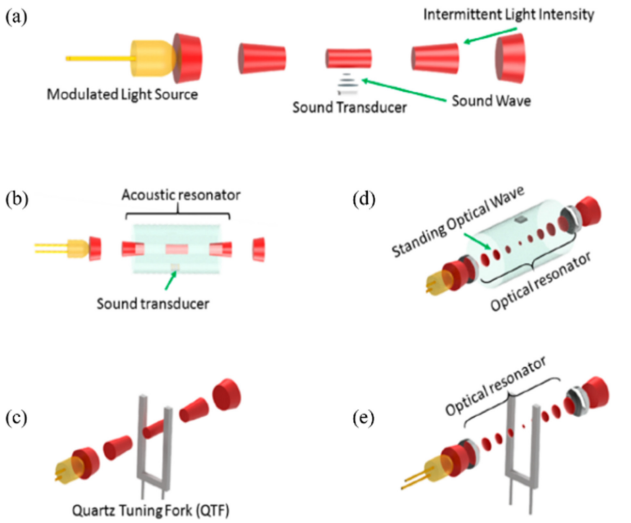

Fig. 2. Schematics of various main photoacoustic spectroscopy (PAS) structures (direct types). Adapted from [1].

Thus, the output of the PAS gas sensor increases with the optical path length, signal quality, sensitivity of the acoustic sensor, energy of the irradiated light, absorption coefficient of the gas, and concentration of the target gas. It is inversely proportional to the volume of the sensor cell and angular frequency.

Fig. 2 illustrates the configuration and types of direct-type PAS gas sensors. The basic components include a light source (microelectromechanical system (MEMS) radiator, light-emitting diode (LED), laser), resonating structure, and acoustic sensor. The structure typically includes a resonator, such as a quartz tuning fork or cantilever, within the optical waveguide.

Indirect-type PAS gas sensors, as shown in Fig. 3, do not require optical waveguides (Fig. 3 (a)) or waveguides with a resonant structure (Fig. 3 (b)). LEDs, lasers, MEMS structures, and filament-based infrared emitters are used as infrared light sources. The optical filter used in this configuration either passes the absorption wavelength of the target gas or uses CaF_2 as an infrared window to pass the entire wavelength of the radiated infrared light. The infrared detector, target gas, microphone, temperature sensor (NTC or temperature IC), and photodiode are sealed in the same package [26]. The main advantage of this type is the flexibility in choosing the target gas by only exchanging the gas in the package.

When infrared light is irradiated externally, the target gas inside the package undergoes thermal vibrations, causing the microphone, which serves as an acoustic sensor, to measure the acoustic pressure changes (sensitivity = 0.074 μV/ppm, limit of detection (LOD) = 2.2 ppm) and provide output signals. According to recent research by the IMTEK group, the theoretical

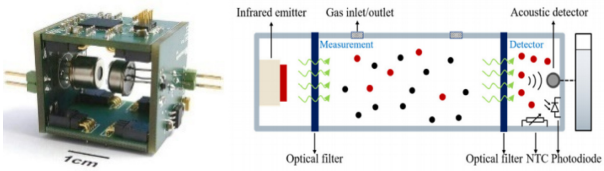

(a) (b)

Fig. 3. Schematics of indirect-type photoacoustic gas sensor: without (a) and with (b) optical waveguides. Reprinted with permission from Ref. [25] Copyright (2015) Elsevier, Ref. [26] Copyright (2023) IEEE.

LOD of an indirect-type PAS sensor structure using LIAs ranges from 37 ppb to 2.2 ppm [26,27]. In another study, the same group introduced a PAS sensor that actively analyzed environmental information by implementing machine learning [28,29]. However, the indirect type generally shows a high LOD compared to direct PAS gas sensors because its response is affected by the exponential function of light intensity.

When filaments or MEMS heating elements are used as infrared emitters, the light output is relatively low at the absorption wavelengths, and the large thermal mass prevents the emission of pulse signals at frequencies above certain thresholds (e.g., 20 Hz). Another limitation is the difficulty in securing microphones that can detect acoustic signals at low frequencies, although advancements in MEMS technology have provided microphones with a roll-off frequency of approximately 7 Hz [30]. It has also been reported that the voltage output from microphones changes in response to variations in temperature and pressure, resulting in frequency shifts in the acoustic pressure signal [31-34].

2.2. Types and Characteristics of Resonant Cells in PAS Gas Sensors

In this section, we discuss the types of resonant structures used in PAS gas sensors and their design parameters and characteristics. Fig. 4 shows the most commonly used PAS cells for fabricating PAS gas sensors.

A typical PAS cell has a tube or pipe shape, and when its cross-sectional area is small compared to the length, acoustic pressure occurs along the direction of light propagation or the length of the pipe. Therefore, the tube or pipe is a one-dimensional resonant structure. Examples of such structures are shown in Fig. 4 (a) and (b). The acoustic pressure generated inside the tube has opposite or identical phases at the open and closed parts, and standing waves are formed through repeated reflections. In Fig. 4 (a), when both ends of the pipe are open (or one end is open and the other

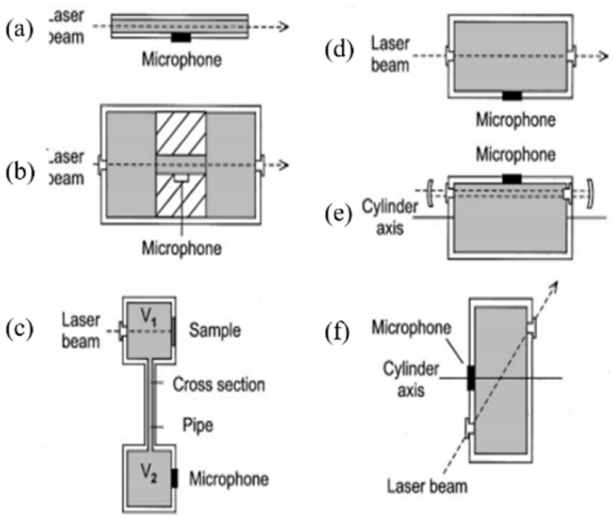

Fig. 4. Fundamental resonating structures of PAS cells. Reprint with permission from Ref. [21] Copyright (2001) AIP Publishing.

is closed) and the length of the pipe is an integer multiple of half the wavelength of the sound (i.e., an odd multiple of a quarter wavelength), resonance occurs inside the pipe. The relationship among the resonant frequency, sound velocity, and pipe length can be expressed using Eqs. (2) and (3) [21,35]. The structure shown in Fig. 4 (b) is similar to that shown in Fig. 4 (a) and is referred to as an H-type resonator. In this case, the buffer length is set to one-quarter of the standing wave [16,19,31,35], and the radius is designed to be 2.5–3 times the radius of the resonant tube [19].

$$f_n = \frac{nc}{2(l+\Delta l)} \tag{2}$$

$$f_{2m-1} = \frac{(2m-1)c}{4(l+\Delta l)} \tag{3}$$

where n & m=1,2,3, … , c and l are the speed of sound and the length of the resonator, respectively, and Δl is the so-called end correction factor, which should be added to the total length of the resonator.

Fig. 4 (c) shows a Helmholtz resonator structure, which consists of a chamber (or cavity, V_1) where infrared light is irradiated and a second chamber (V_2) with acoustic pressure of the opposite phase [36-39]. The structure is composed of two cavities connected by a capillary or neck, and the resonant frequency is expressed by Eq. (4).

$$f_r = \frac{c}{2\pi}\sqrt{\frac{A}{Vl}} \tag{4}$$

where l, A, V are the length of the tube, cross-sectional area of the capillary, and volume of the cavity, respectively. The volume

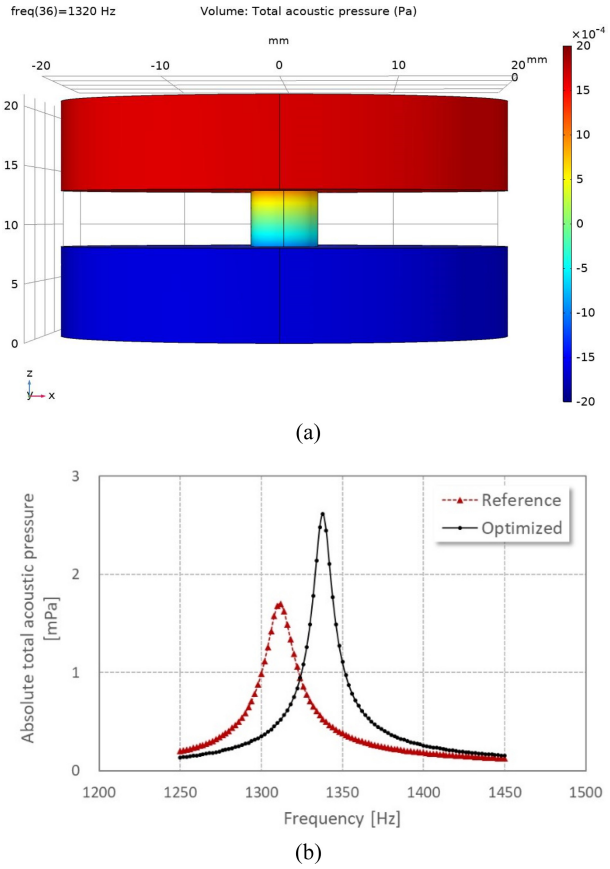

Fig. 5. Simulation results of differential Helmholtz resonator: (a) acoustic pressure distributions, (b) resonant frequencies compared to previous results [39].

should be replaced with the effective volume defined in Eq. (5).

$$V_{eff.} = \frac{1}{(1/V_1)+(1/V_2)} \tag{5}$$

Fig. 5 shows the acoustic pressure generated by the differential Helmholtz resonator under infrared irradiation. As shown in Fig. 5, the acoustic pressure in the upper chamber reaches 1.46 mPa, and the resonant frequency is 1320 Hz. The simulated results show differences of 3.4% in resonant frequency and −43% in sound pressure compared with the results from Li et al. [38].

The most frequently used PAS cell is the cylindrical resonator, as shown in Fig. 4 (d)–(f) (radial mode (d), azimuthal mode (e), and first radial mode (f)). The resonant frequencies of the lossless cylindrical resonator are given by Eq. (6) [21].

$$f_{jmq} = \frac{c}{2}\left[\left(\frac{\alpha_{jm}}{R}\right)^2 + \left(\frac{q}{L}\right)^2\right]^{1/2} \tag{6}$$

where R and L denote the radius and length of the cylinder, respectively. The indices jmq (nonnegative integers) refer to the

eigenvalues of the radial, azimuthal, and longitudinal modes. α_{jm} is the j-th zero of the derivative of the m-th Bessel function divided by π.

In terms of the fabrication of a compact PAS cell and the required resonant frequency, the Helmholtz resonator is more compact than the H-type resonating structure. Furthermore, by using a laser as a light source and irradiating the wall of the Helmholtz resonator, as reported by Li et al. [38], the optical path can be increased within a small volume of the PAS cell. Therefore, the Helmholtz resonator is an efficient candidate for high-performance PAS cells.

2.3. Enhancement of Properties of PAS Gas Sensors

As presented in Eq. (1), the output of the PAS gas sensor increases in proportion to 1) the absorption coefficient of the target gas, 2) energy of the incident light, 3) length of the optical path, 4) quality factor (signal quality), and 5) sensitivity of the acoustic sensor. It decreases in inverse proportion to the frequency and volume of the cell. From a physical perspective, the absorption coefficient of the target gas cannot be adjusted during system design. Therefore, when designing a system, the focus should be on improving the sensitivity of the acoustic pressure sensor, securing sufficient light energy, increasing the optical path length while reducing the volume, and adjusting the frequency to lower values while improving the quality factor (Q factor) during the resonant structure or signal processing stages.

Furthermore, because the changes in acoustic pressure caused by sub-ppm concentrations of gases result in ultra-low signals in the pico- to nano-voltage range, it is essential to consider extremely weak signals from external noise sources (e.g., power noise, vibrations, and thermal noise). Therefore, measures should be taken to enhance the initial acoustic pressure signals. This section explores several parameters for improving the acoustic pressure output of PAS gas sensors.

2.3.1. Radiation Source and Powers

The infrared light sources used in PAS gas sensors include MEMS-based infrared light sources [23,25,40], LEDs [18,19,31], and lasers [16,24,32,38,40]. When using filament- or MEMS-based light sources, mechanical energy transfer has a significantly higher effect (by approximately two orders of magnitude) than electrical chopping methods [40]. Using a laser that emits infrared light at the same wavelength as the absorption wavelength of the target gas is more effective than mechanical chopping. Recently, lasers have been available in a wavelength range from 2.8 to 6.5 μm, which means that a highly efficient PAS gas sensor could be fabricated with high power, over 10 mW at the central wavelength [41]. Although using a laser can enhance the sensitivity of PAS gas sensors, it is important to consider that the complexity of the circuit design and cost may increase. Furthermore, the wavelength range of a laser is very narrow compared to that of thermal radiators; therefore, it is difficult to construct a multigas analyzer. The high cost is another challenge in the fabrication of PAS gas sensors using a laser source. However, by combining tunable diode lasers (or multiple lasers) and PAS cells, high-performance and multi-gas PAS sensors can be fabricated for diagnostic purposes in many areas.

2.3.2. Optical Path Length and Resonant Structures

The resonant structures used in PAS gas sensors include 1) short optical paths, such as H-type, T-type, Helmholtz resonators (HRs), and differential Helmholtz resonators (DHRs), and 2) long optical path structures, such as integrating spheres and Herriot cells. As the optical path length increases, the output signal increases according to Eq. (1). For example, in the H-type, a retroreflection cavity structure can be used to double the optical path length [42]. Using this structure, the signal size was increased by a factor of 3.55, and two microphones were installed in the two cavities to allow differential amplification.

In the Helmholtz structure, laser irradiation at a specific angle to the central axis of the cylinder increases the number of reflections of the incident light, resulting in a significant enhancement of the optical path length. With 6 mW laser power, the LOD for methane gas was reported to be 177 ppb [38]. Although the Helmholtz structure generally has a lower sensitivity than other structures [21], this limitation can be overcome by increasing the optical path length. Another study using a Herriot cell structure showed a dramatic increase in the optical path length, improving the LOD to below 10 ppb [43]. Zhang et al. [44] reported using a Herriot cell with 29 reflections, providing an optical path of approximately 0.61 m with an Allan deviation of 0.0089 μV, and an LOD of 12.2 ppb.

One structure that can increase the optical path length is an integrating sphere. Li et al. [24] demonstrated that an integrating sphere with a radius of 5.08 cm and a resonator length of 1.8 cm could achieve an LOD of 0.27 ppb.

In this study, we proposed improvements to the existing optical waveguide [45] and performed simulations to verify its potential for use in PAS gas sensors. The results are shown in Fig. 6. In the white cell, we observed a different distribution of heat generated

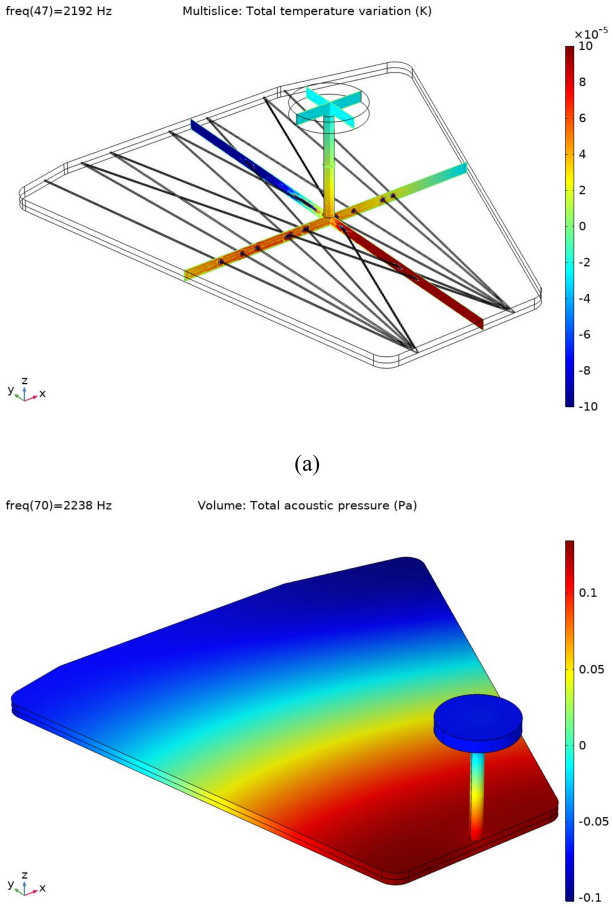

(a)

(b)

Fig. 6. Newly proposed PAS cell structure: (a) optical path, (b) resonator positioned at the edge where the generated heat is high [46].

by infrared light in regions with and without repeated reflections. We also observed that the acoustic pressure in the region where the microphone was installed had a phase opposite to that inside the PAS cell. By reducing the volume while maintaining a constant optical path length (0.98 m), we confirmed that the acoustic pressure generation could be enhanced.

3. CHARACTERISITCS AND COMPONENTS OF LOCK-IN AMPLIFIERS (LIAs)

3.1 Basic Structures of LIAs

Fig. 7 shows a block diagram of the LIA circuits. A basic LIA consists of a phase-sensitive detector (PSD) and a low-pass filter (LPF). To extract the sound pressure signal buried in noise (ranging from a few pPa to tens of nPa), the circuit includes 1) a

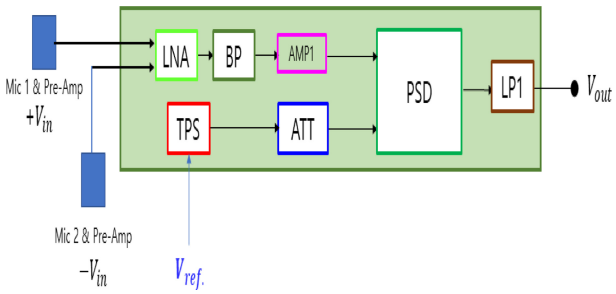

Fig. 7. Block diagram of Lock-in amplifier circuits.

low-noise amplifier (LNA) for the differential amplification of two acoustic sensor signals, 2) a band-pass filter (BP), and 3) a tunable phase shifter (TPS) along with a comparator (ATT).

The phase-sensitive detector multiplies two signals; for example, multiplying the sound pressure signal (which is periodic) with a reference signal results in an output voltage expressed through the trigonometric product formula. When the frequencies of the sound pressure and reference signals are the same, their product follows the relationship shown in Eq. (7):

$$V_{sig.} \times V_{ref.} = \frac{1}{2} A_{sig.} A_{ref.} [\cos(\theta_{sig.} - \theta_{ref.}) - cos(2\omega t + \theta_{sig.} + \theta_{ref.})] \quad (7)$$

where $A_{sig.}$ and $A_{ref.}$ are the amplitudes of the sound pressure and reference signals, respectively, ω is the angular frequency, $\theta_{sig.}$ is the phase of the sound pressure signal, and $\theta_{ref.}$ denotes the phase of the reference signal.

3.2 Categories and Properties of LIAs

The output of the multiplication process in Eq. (7) includes 1) a DC component owing to the phase difference, and 2) an AC component corresponding to the second harmonic of the reference frequency. To extract signals such as sound pressure, magnetic fields, small resistances, or small capacitances from noise accurately, the circuit configuration is determined by how precisely the amplitude and phase of the signals can be locked in. This can be achieved using 1) phase–voltage converters [47-50], and 2) vector analysis methods [51-57], as explained below.

3.2.1. Phase–Voltage Converting Methods

Fig. 8 shows a block diagram of the phase–voltage converting (PVC) method. The PAS sensors, which use microphones as acoustic sensors, have two microphones for differential amplification. The signals from Mic1 and Mic2 are differentially

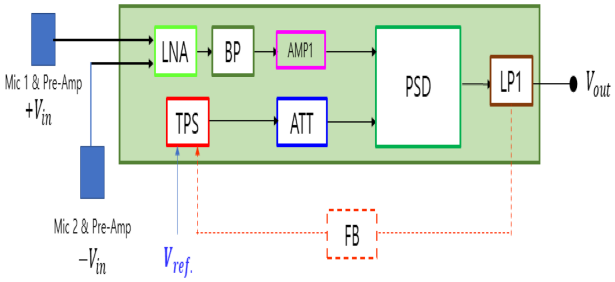

Fig. 8. Block diagram of the phase–voltage converting method.

amplified using an LNA and passed through a BP to obtain the sound pressure signal at the resonant frequency. As shown in Fig. 8, the measured and amplified voltage signal is input to the PSD along with the reference signal. The reference signal entering the PSD is phase shifted by 90° using a TPS before being supplied to the PSD.

After passing through the PSD, the second harmonic and DC components of the input signal frequency are obtained, and an LPF is used to filter out the high-frequency noise, resulting in a DC output voltage proportional to the measured gas concentration. However, if the frequency and phase of the measured sound pressure signal are not aligned precisely, accurate gas concentration measurements cannot be obtained, as shown in Eq. (7). Therefore, accurate phase alignment and precise frequency measurement of the reference signal are crucial. When the circuit is in its initial state, as shown in Eq. (8), a reference signal with the same frequency as the measured signal is provided to the TPS, as presented in Eq. (9):

$$V_{sig.} = A\sin(\omega t + \theta_{sig.}) \tag{8}$$

$$V_{ref.} = B\sin(\omega t + \theta_{ref.}) \tag{9}$$

The phase difference between the input signal and the reference signal is given by: $\Delta\theta = \theta_{sig.} - \theta_{ref.}$

Through the PSD operation, the multiplication of the input and reference signals results in a DC signal after the LPF that is independent of frequency. The output voltage is expressed in Eq. (10):

$$V_{psd} = \frac{1}{2}AB[\cos(\Delta\theta) - \cos(2\omega t + \theta_{sig.} + \theta_{ref.})] \tag{10}$$

Therefore, the output signal passing through the LPF may be distorted because of the phase difference. To correct this, feedback signals (FB) can be used in conjunction with an analog multiplier (such as AD633) and a phase-shifter circuit, forming a TPS or quadrature phase shifter. This compensates for the phase difference between the sensor and reference signals. The FB

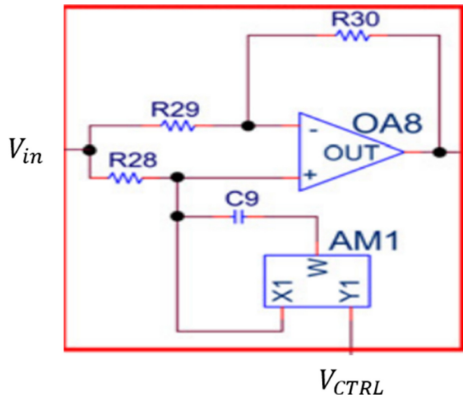

Fig. 9. Schematics of tunable phase shifter. Reprinted with permission from Ref. [50] Copyright (2013) Elsevier.

affects the phase shift in the TPS [58], ensuring that the phase difference remains at exactly 90°, according to Eqs. (11) and (12), respectively.

$$C_{eq.} = C_9\left(1 - \frac{1}{10}V_{CTRL}\right) \tag{11}$$

$$\angle\left(\frac{V_{tps,out}}{V_{tps,ref.}}\right) = -2arctan(\omega R_{28}C_{eq.}) \tag{12}$$

The resulting PSD output is given by Eq. (13) and (14) as follows:

$$V_{ref.(tps)} = B\sin(\omega t + \theta_{ref.} + 90) = B\cos(\omega t + \theta_{ref.}) \tag{13}$$

$$V_{sig.} \times V_{ref.(tps)} = AB\sin(\omega t + \theta_{sig.})\cos(\omega t + \theta_{ref.}) \tag{14}$$

Thus, the PSD output can be expressed as Eq. (15):

$$V_{psd} = \frac{1}{2}AB[\cos\Delta\theta - \cos(2\omega t + \theta_{sig.} + \theta_{ref.})] \tag{15}$$

When the sensor and reference signals have identical frequencies and phases, the PSD output is zero after passing through the LPF. This condition is expressed in Eq. (16):

$$V_{out} = \frac{1}{2}A\cos(-90) \tag{16}$$

The final circuit, that is, the output signal passing through the LPF in the LIA, is given by Eq. (17), which includes the amplification factor (Δ), reference signal amplitude ($M_{ref.}$), and pressure signal amplitude (A) from the microphones:

$$V_{out} = \Delta \times \frac{2}{\pi}AM_{ref.} \tag{17}$$

However, as pointed out by De Marcellis et al. [49], for

automatic phase alignment, multiple TPS devices must be connected in series, which increases the cost and the circuit complexity and may hinder their application in portable gas sensors.

3.2.2. Vector Analysis (VA) Methods.

The output voltage of the PSD, as shown in Eq. (15), consists of terms corresponding to the phase difference and second harmonic component. When the reference signal is provided with the same frequency and phase as the input signal, the amplitude ±1 signal is output, the PSD provides a phase-sensitive rectified version of the sensor signal, and by using an LPF, the harmonic components containing noise are removed. The amplitude of the sensor signal is then extracted as shown in Eq (18):

$$V_{output} = \frac{2}{\pi} A_{sen.} \cos\theta \tag{18}$$

where $A_{sen.}$ is the amplitude of the input signal, and θ is the phase difference between the sensor signal and the reference signal.

However, Eq. (18) does not provide information on the phase difference. Consequently, the magnitude of the sensor output cannot be accurately determined. Therefore, another PSD circuit is required to provide a reference signal with a 90° phase shift relative to the sensor signal, enabling accurate measurement of the amplitude and phase differences. This function is provided by a dual-branch LIA [52-56], as shown in Fig. 10.

Fig. 10 shows the schematic of a dual-branch LIA circuit. By providing two PSDs with reference signals of the same frequency and a 90° phase shift between them, the components of the vector along the axes can be calculated as shown in Eqs. (19) and (20), respectively.

$$V_{psd,0} = \frac{1}{2} A_{sen.} \cos(\theta_{sig.} - \theta_{ref.}) \tag{19}$$

$$V_{psd,90} = \frac{1}{2} A_{sen.} \sin(\theta_{sig.} - \theta_{ref.}) \tag{20}$$

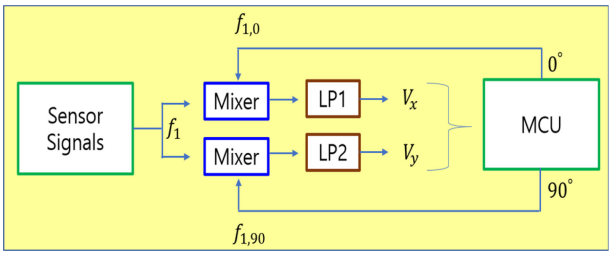

Fig. 10. Schematics of a dual-branch LIA circuit.

When the phase difference is $\Delta\theta$, the average values of the DC voltage signals from each branch are given by Eq. (21):

$$V_x = \frac{2}{\pi} A_{sen.} \cos\Delta\theta, \quad V_y = \frac{2}{\pi} A_{sen.} \sin\Delta\theta \tag{21}$$

From Eq. (21), although the phase difference changes, the amplitude and phase difference of the sensor signal can be accurately calculated using Eq. (22):

$$A_{sen.} = \frac{\pi}{2}\sqrt{V_x^2 + V_y^2}, \quad \theta = arctan\left(\frac{V_y}{V_x}\right) \tag{22}$$

An example of applying LIAs to gas sensors was presented by De Marcellis et al. [47-50], who used an oxide semiconductor gas sensor and a load-resistance circuit with a frequency signal. The response characteristics were measured based on gas concentration by inputting the output voltage from the load resistance into the LIA. Using this circuit, they reported a resolution of 500 ppb, distinguishing sensor signals on the order of a few hundred nanovolts. Similarly, Keeratiraee et al. [59] applied another LIA to a PAS gas sensor for NO_2 measurement and achieved an LOD of approximately 100 ppb.

In this section, the two LIA circuits are discussed and reviewed to distinguish their technical advantages. Although the PVC method has a unique and auto-calibrating feature of the phase difference between the sensor and reference signals, the circuit requires cascade PVC components to achieve this requirement. In contrast, VA methods are very simple in terms of the relevant circuitry, so they are very cost effective, which could be the reason why the circuitry of VA methods is designed and implemented in integrated circuit chips [54].

4. DISCUSSIONS AND CONCLUSIONS

In this study, we explored the key components of PAS gas sensors, focusing on the resonant cell and LIA used for signal analysis. To improve the performance of the PAS gas sensors, we examined methods based on mathematical models, such as increasing the energy of the laser light source to match the absorption wavelength of the target gas. This approach allowed us to assess the potential of analyzing gases at concentrations below the ppm level. Although MEMS IR light sources and LEDs have been increasingly applied in portable or battery-operated sensors, laser applications in monitoring and analyzing ppb-level gases have become a significant trend. However, for portable and battery-powered operations, indirect PAS gas sensors are more

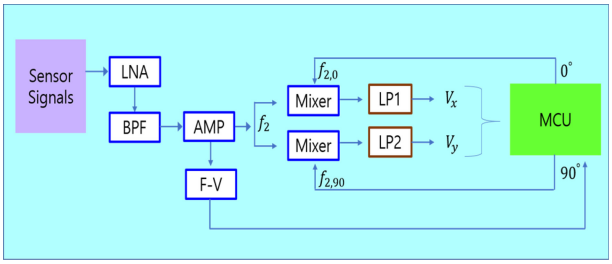

Fig. 11. Block diagram of active-LIA for PAS gas sensor.

favorable with pulsed radiators (e.g., MEMS IR sources or LEDs) in field applications.

For resonant cells, methods for increasing the optical path length in basic cells or using integrating spheres and Herriot cells can be considered. However, it is worth noting that integrating spheres and Herriot cells tend to be bulky, which runs counter to the trend of miniaturization. The white cell-based resonator suggested in this study could be a promising candidate for high-performance PAS cells because it has a small volume (16915.4 mm^3) and a large optical path length (approximately 0.98 m). Other efforts are being made to reduce the volume of resonant cells and adopt ultra-small resonators, such as quartz resonators or cantilevers, for miniaturization. However, the resonant frequency depends on the ambient temperature; therefore, auto-tuning of the reference signal frequency is promising for the stable and reliable operation of PAS gas sensors.

In terms of signal detection, the LIA circuit shown in Fig. 10 must undergo several modifications to be applicable to PAS gas sensors. The structure proposed by Keeratiraee et al. [59], which uses a single PSD, does not provide accurate sensor signals. To address this limitation, an alternative structure is proposed, as shown in Fig. 11. Specifically, when sound pressure at frequency of f_2 is generated by infrared irradiation in the PAS gas sensor, it is first amplified using an LNA. The signal is further amplified using a BP and a secondary amplifier. The amplified signal is then sent to the microcontroller unit (MCU) via a frequency-to-voltage converter, and another signal is input into the two mixers for vector analysis. The voltage input to the MCU is compared to a lookup table or other data to accurately determine the frequency and generate a reference signal. This reference signal, along with a square wave and a 90° out-of-phase signal (amplitude ±1), is supplied to the mixers. By processing the output from the multiplier through LPFs (LP1 and LP2) to obtain the vector signals, the amplitude and phase of the sensor signal can be precisely determined using Eqs. (21) and (22), resulting in a more accurate sensor output.

This study examined two critical components for the research and development of PAS gas sensors: the PAS cell and LIA. In the development of PAS gas sensors, the choice of the PAS cell should align with the design of the system. The incorporation of LIAs using vector analysis techniques is recommended to simplify the circuit design. The fabrication of ASIC chips of LIAs for multiple purposes, including PAS and oxide semiconductor gas sensors, would improve the performance of gas sensors. In addition, implementing analog–digital circuits that can provide a square-wave reference signal through the MCU would be beneficial for optimal performance in the signal processing of sensors.

ACKNOWLEDGMENT

This study was supported by Korea National University of Transportation in 2024.

REFERENCES

[1] Stefan Palzer, “Photoacoustic-based gas sensing: A review”, *Sens.*, Vol. 20, No. 9, p. 2745, 2020.
[2] J. S. Li, W. D. Chen, and B. L. Yu, “Recent progress on infrared photoacoustic spectroscopy techniques”, *Appl. Spectrosc. Rev.*, Vol. 46, No. 6, pp. 440-447, 2011.
[3] E. L. Kerr and J. G. Atwood, “The laser illuminated absorptivity spectrophone: A method for measurement of weak absorptivity in gases at laser wavelengths”, *Appl. Optic.*, Vol. 7, No. 5, pp. 915-921, 1968.
[4] L. B. Kreuzer, “Ultra-low gas concentration infrared absorption spectroscopy”, *J. Appl. Phys.*, Vol. 42, No. 7, pp.2934-2943, 1971.
[5] J. H. Kim and S. H. Yi, “Effects of temperature and humidity on NDIR CO2 gas sensor”, *J. Sens. Sci. Technol.*, Vol. 26, No. 3, pp. 179-185, 2017.
[6] S. H. Yi, “Infrared light absorbance: A new method for temperature compensation in nondispersive infrared CO2 gas sensor”, *J. Sens. Sci. Technol.*, Vol. 29, No. 5, pp. 303-311, 2020.
[7] J. S. Park and S. H. Yi, “Temperature compensated NDIR CH_4 gas sensor with focused beam structure”, *Procedia Eng.*, Vol. 5, pp.1248-1251, 2010.
[8] S. H. Yi, “Temperature compensated methods of nondispersive infrared CO_2 gas sensor with dual elliptical optical waveguide”, *Sens. Mater.*, Vol. 29, No. 3, pp. 243-252, 2017.
[9] J. H. Kim, H. C. Cho, and S. H. Yi, “Temperature compensation and characteristics of non-dispersive infrared alcohol sensor according to the intensity of light”, *J. Sens. Sci. Technol.*, Vol. 27, No. 1, pp. 47-54, 2018.
[10] H. Hussain, J. H. Kim, and S. H. Yi, “Characteristics and

temperature compensation of non-dispersive infrared (NDIR) alcohol gas sensors according to incident light intensity", *Sens.*, Vol. 18, No. 9, p. 2911, 2018.

[11] B. HoK, H. Pettersson, A. K. Andersson, S. Haasl, and P. Akerlund, "Breath analyzer for alcoIocks and Screening devices", *IEEE Sens. J.*, Vol. 10, No. 1, pp.10-15, 2010.

[12] G. H. Lee and S. H. Yi, "Fault analysis of transformer using tunable infrared gas sensors", *J. Sens. Sci. Technol.*, Vol. 32, No. 1, pp. 55-61, 2023.

[13] T. Chen, F. Ma, Y. Zhao, Y. Zhao, L. Wan, K. Li, and G. Zhang, "Portable ppb-level acetylene photoacoustic sensor for transformer on-field measurement", *Optik*, Vol. 243, p. 167440, 2021.

[14] S. H. Yi, "Analysis of biomarkers with tunable infrared gas sensors", *J. Sens. Sci. Technol.*, Vol. 30, No.5, pp. 314-319, 2021.

[15] C. Chen, Q. Ren, and Y. Z. Wang, "Review on multi gas detector using infrared spectral absorption technology", *Appl. Spectrosc. Rev.*, Vol. 54, No. 5, pp. 425-444, 2019.

[16] F. Wang, Y. Cheng, Q. Xue, Q. Wang, R. Liang, J. Wu, J. Sun, C. Zhu, and Q. Li, "Techniques to enhance the photoacoustic signal for trace gas sensing: A review", *Sens. Actuators A Phys.*, Vol. 345, p. 113807, 2022.

[17] J. Uotila, V. Koskinnen, and J. Kauppinen, "Selective differential photoacousitc method for trace gas analysis", *Vib. Spectrosc.*, Vol. 38, No. 1-2, pp.3-9, 2005.

[18] H. F. Pernau, K. Schmitt, J. Huber, S. Rademacher, A. Eberhardt, and J. Wollenstein, "Resonant photoacoustic CO2 spectroscopy with LED light source", *Procedia Eng.*, Vol. 168, pp. 1325-1328, 2016.

[19] L. A. Ishaku and D. Hutson, "A resonant photoacoustic CO2 sensor based on Mid-IR LED and MEMS microphone technology operating at 4.3 μm", *Innovative Syst. Des. Eng.*, Vol. 7, No. 8, pp. 1-11, 2016.

[20] F. Yehya and A. K. Chaudhary, "Designing and modeling of efficient resonant photoacoustic sensors for spectroscopic applications", *J. Modern Phys.*, Vol. 2, pp. 200-209, 2011.

[21] A. Miklos, P. Hess, and Z. Bozoki, "Application of acoustic resonators in photoacoustic trace gas analysis and metrology", *Rev. Sci. Instrum.*, Vol. 72, No. 4, pp. 1937-1955, 2001.

[22] S. H. Yi, J. S. Kim, and S. U. Yi, "Analysis of Biomarkers using optical electronic-nose", *J. Sens. Sci. Technol.*, Vol. 28, No. 3, pp. 171-176, 2019.

[23] W. Cai, J. Tang, L. Cheng, C. Zhang, M. Fan, Q. Zhou, and Q. Yao, "Detection of SF decomposition under partial discharge by photoacoustic spectroscopy and its temperature characteristics", *IEEE Trans. Instrum. Meas.*, Vol. 65, pp. 1343-1351, 2016.

[24] Z. Li, G. Si, Z. Ning, J. Liu, Y. Fang, B. Si, Z. Cheng, and C. Yang, "Highly sensitive sphere-tube coupled photoacoustic cell suitable for detection of a variety of trace gases: NO2 as an example", *Sens.*, Vol. 22, No. 1, p. 281, 2022.

[25] J. Huber, A. Ambs, and J. Wollenstein, "Miniaturized photoacoustic carbon dioxide sensor with integrated temperature composition for room climate monitoring", *Procedia Eng.*, Vol. 120, pp. 283-288, 2015.

[26] N. Zhang, A. Srivastava, X. Li, Y. Li, Z. Zhou, A. Bittner, X. Zhou, and A. Dehe, "Design and evaluation of a miniaturized non-resonant photoacoustic CO_2 gas sensor with integrated electronics", *Proc. of 2023 IEEE Sens.*, pp. 1-4, Vienna, Austria, 2023.

[27] A. Srivastava, Y. Tian, A. Bittner, and A. Dehé, "Design and characterization of macroscopic indirect photoacoustic gas sensor", *Proc. of 2022 IEEE Sens.*, pp.1-4, Dallas, USA, 2022.

[28] A. Srivastava, P. Sharma, A. Sikora, A. Bittner, and A. Dehé, "Data-driven modelling of an indirect photoacoustic carbon dioxide sensor", *Proc. of 2024 IEEE Appl. Sensing Conf.* (APSCON), p.1-4, Goa, India, 2024.

[29] A. Srivastava, P. Sharma, A. Sikora, A. Bittner, and A. Dehé, "Temporal behavior analysis for the impact of combined temperature and humidity variations on a photoacoustic CO_2 sensor", *Proc. of 2024 IEEE Appl. Sensing Conf.* (APSCON), pp.1-4, Goa, India, 2024.

[30] https://www.knowles.com/ (retrieved on Dec. 12, 2024).

[31] L. A. Ishaku, D. Hutson, D. Gibson, "Temperature effects on photoacoustic carbon dioxide sensor developed using Mid-IR LED", *Proc. of IEEE Int. Instrum. Technol. (I2MTC)*, pp. 1-6, Huston, USA, 2018.

[32] J. Pangerl, M. Muller, T. Ruck, S. Weigl, and R. Bierl, "Characterizing a sensitive compact mid-infrared photoacoustic sensor for methane, ethane and acetylene detection considering changing ambient parameters and bulk composition (N_2, O_2 and H_2O)", *Sens. Actuators B Chem.*, Vol. 352, p. 13096207, 2022.

[33] R. H. Vafaie, R. S. Pour, S. Nojavan, and K. Jermsittiparert, "Designing a miniaturized photoacoustic sesnor for detecting hydrogen gas", *Int. J. Hydrogen Energy*, Vol. 45, No. 41, pp. 21148-21156, 2020.

[34] J. Wang, M. Chen, Q. Chen, and H. Wang, "A resonant photoacoustic cell for hydrogen gas detection", *Int. J. Hydrogen Energy*, Vol. 47, pp. 35940-35946, 2022.

[35] Z. Gong, K. Chen, Y. Chen, L. Mei, and Q. Yu, "Integration of T-type half-open photoacoustic cell and fiber-optic acoustic sensor for trace gas detection", *Opt. Express*, Vol. 27, No. 13, pp. 18222-18231, 2019.

[36] K. Song, H. K. Cha, V. A. Kapitanov, Yu. N. Ponomarev, A. P. Rostov, D. Courtois, B. Parvitte, and V. Zeninari, "Differential Helmholtz resonant photoacoustic cell for spectroscopy and gas analysis with room-temperature diode lasers", *Appl. Phys. B*, Vol. 75, pp. 215-227, 2002.

[37] K. Tachibana, K. Okada, R. Kobayashi, and Y. Ishihara, "Development of a high-sensitivity and portable cell using Helmholtz resonance for noninvasive blood glucose-level measurement based on photoacoustic spectroscopy", *Proc. of 38th Annu. Int. Conf. IEEE Eng. Med. Biol. Soc.* (EMBC), pp. 6477-6480, Orlando, USA, 2016.

[38] Z. Li, J. Liu, G. Si, Z. Ning, and Y. Fang, "Design of a high-sensitivity differential Helmholtz photoacoustic cell and its application in methane detection", *Opt. Express*, Vol. 30, No. 16, pp. 28984-28996, 2022.

[39] J. H. Gil, S. O. Han, and S. H. Yi, "Simulation of Differential Helmholtz Resonator for PAS Gas Sensor", *Proc. of 2024 Fall Conf. Kor. Sens. Soc.*, p. 487, Yeosu, Korea,

2024.
[40] J. Uotila, "Comparison of infrared sources for a photoacoustic gas detection system", *Infrared Phys. Technol.*, Vol. 51, pp. 122-130, 2007.
[41] https://www.nanoplus.com/ (retrieved on Dec. 13, 2024).
[42] C. Zhang, S. Qiao, and Y. Ma, "Highly sensitive photoacoustic acetylene detection based on differential photoacoustic cell with retro-reflection-cavity", *Photoacoustics*, Vol. 30, p. 100467, 2023.
[43] K. Chen, S. Liu, B. Zhang, Z. Gong, Y. Chen, M. Zhang, H. Deng, M. Guo, F. Ma, F. Zhu, and Q. Yu, "Highly sensitive photoacoustic multi-gas analyzer combined with mid-infrared broadband source and near-infrared laser", *Opt. Lasers Eng*., Vol. 124, pp. 105844, 2020.
[44] M. Zhang, B. Zhang, K. Chen, M. Guo, S. Liu, Y. Chen, Z. Gong, Q. Yu, Z. Chen, and M. Liao, "Miniaturized multipass cell based photoacoustic gas sensor for parts-per-billion level acetylene detection", *Sens. Actuators A Phys*., Vol. 308, p. 112013, 2020.
[45] S. H. Yi, G. H. Lee, H. G. Yeo, and J. H. Kim, "Non-dispersive infrared sensor deposited hydrophobic thin film", KR 10-1907393, 05 Oct., 2018.
[46] S. H. Yi, S. O. Han, and H. G. Yeo, "The circuits and components for photoacoustic gas sensors", Korean Patent 10-2024-0173544, 28 Nov., 2024.
[47] A. De Marcellis, A. Di Giansante, G. Ferri, C. Di Natale, E. Martinelli, and A. D. Amico, "Analog automatic lock-in amplifier for very low gas concentration detection", *Procedia Eng*., Vol. 5, pp. 200-203, 2010.
[48] A. De Marcellis, G. Ferri, and E. Palange, "A novel analog automatic phase-voltage converter for signal phase-shifting detection", *IEEE Sens. J*., Vol. 11, No. 2, pp. 259-266, 2011.
[49] A. De Marcellis, G. Ferri, A. D'Amico, C. Di Natale, and E. Martinelli, "A fully-analog lock-in amplifier with automatic phase alighment for accurate measurments of ppb gas concentrations", *IEEE Sens. J*., Vol. 12, No. 5, pp. 1377-1383, 2012.
[50] A. De Marcellis, G. Ferri, and E. Palange, "High sensitivity, high resolution, uncalibrated phase read-out circuit for optoelectronic detection of chemical substances", *Sens. Actuators B Chem*., Vol. 179, pp. 328-335, 2013.
[51] E. J. Kim, H. Y. Park, and S. K. Kim, "Low frequency clock synchronization technique for low signal to noise ratio (SNR) signal recovery from noise environment", *Proc. of 2009 16th Int. Conf. Digital Signal Process.*, pp.1-4, Santorini, Greece, 2009.
[52] M. Gabal, N. Medrano, B. Calvo, P. A. Martinez, S. Celma, and M. R. Valco, "A complete low voltage analog lock-in amplifier to recover sensor signals buried in noise for embedded applicaions", *Procedia Eng*., Vol. 5, pp. 74-77, 2010.
[53] A. D'Amico, A. De Marcellis, C. Di Carlo, C. Di Natale, G. Ferri, E. Martinelli, R. Paolesse, and V. Stornelli, "Low-voltage low-power integrated analog lock-in amplfier for gas sensor applications", *Sens. Actuators B Chem*., Vol. 144, pp. 400-406, 2010.
[54] C. Azzolini, A. Magnaini, M. Tonelli, G. Chiorboli, and C. Morandi, "A CMOS vector lock-in amplifier for sensor applications", *Microelectronics J.*, Vol. 41, pp. 449-457, 2010.
[55] J. Aguirre, D. Garcia-Romeo, N. Medrano, and B. Calvo, "Square-signal-based algorithm for analog lock-in amplifiers", *IEEE Trans. Ind. Electron.*, Vol. 61, No. 10, pp. 5590-5598, 2014.
[56] G. M. Bobadilla, J. R. Resendiz, G. M. Valtierra, S. Z. Genaro, M. L. Maurino, and G. A. Mariano, "Dual-phase lock-in amplifiers based on FPGA for low-frequencies experiments", *Sens.*, Vol. 16, pp. 379-390, 2016.
[57] X. Xu, Y. Suganuma, and A. A. Dhirani, "Low-cost, high-performance lock-in amplifier for pedagogical and practical applications", *J. Chem. Educ.*, Vol. 97, pp. 1167-1171, 2020.
[58] G. Q. Zhang, R. Bargar, and K. Halle, "Circuits for voltage tunning the parameters of Chua's circuit: Experimental application for musical signal generation", *J. Franklin Inst*., Vol. 331, No. 6, pp. 743-784, 1994.
[59] K. Keeratiraee, J. S. Furter, and P. Hauser, "Low-cost electronic circuitry for photoacoustic gas sensing", *HardwareX*, Vol. 11, p. e00280, 2022.
[60] S. H. Yi, "Photoacoustic cell structure for a photoacoustic gas sensor and signal processing circuit therefor", Korean Patent 10-2025-0001802, 06 Jan., 2025.